

Article

The Study of Soliton Mode-Locked and Bound States in Erbium-Doped Fiber Lasers Based on Cr_2S_3 Saturable Absorbers

Dong Li, Ruizhan Zhai *, Yongjing Wu *, Minzhe Liu , Kun Zhao, Qi Yang, Youwei Dong, Xiaoying Li, Xiaoyang Wu and Zhongqing Jia

Shandong Key Laboratory of Optoelectronic Sensing Technologies/National-Local Joint Engineering Laboratory for Energy and Environment Fiber Smart Sensing Technologies, Laser Institute, Qilu University of Technology (Shandong Academy of Sciences), Jinan 250104, China; minzheliu@sdslaser.cn (M.L.); dongyouwei200003@163.com (Y.D.)

* Correspondence: zrz@vip.sdslaser.cn (R.Z.); yongjingwu@sdslaser.cn (Y.W.)

Abstract: Femtosecond fiber lasers are widely utilized across various fields and also serve as an ideal platform for studying soliton dynamics. Bound-state solitons, as a significant soliton dynamic phenomenon, attract widespread attention and research interest because of their potential applications in high-speed optical communication, all-optical information storage, quantum computing, optical switching, and high-resolution spectroscopy. We investigate the effects of pump power variations on the formation of mode-locked solitons and bound-state solitons in a femtosecond fiber laser with a Cr_2S_3 saturable absorber (SA) through numerical simulations while observing the transition, formation, and break-up process of bound soliton pulses. By optimizing the cavity structure and adjusting the net dispersion, the mode-locked soliton is obtained based on this SA. This is the narrowest solitons produced by this SA to date, exhibiting the smallest time-bandwidth product. Moreover, stable double-bound solitons and unique $(2 + 1)$ triple-bound solitons are successfully obtained. The diverse bound-state solitons not only demonstrate the excellent nonlinear absorption properties of Cr_2S_3 as a saturable absorber but also expand the scope of applications for Cr_2S_3 saturable absorbers in fiber lasers.

Keywords: bound-state solitons; Cr_2S_3 saturable absorber; soliton mode-locking



Academic Editor: Maciej Dems

Received: 21 December 2024

Revised: 7 February 2025

Accepted: 10 February 2025

Published: 16 February 2025

Citation: Li, D.; Zhai, R.; Wu, Y.; Liu, M.; Zhao, K.; Yang, Q.; Dong, Y.; Li, X.; Wu, X.; Jia, Z. The Study of Soliton Mode-Locked and Bound States in Erbium-Doped Fiber Lasers Based on Cr_2S_3 Saturable Absorbers. *Materials* **2025**, *18*, 864. <https://doi.org/10.3390/ma18040864>

Copyright: © 2025 by the authors. Licensee MDPI, Basel, Switzerland. This article is an open access article distributed under the terms and conditions of the Creative Commons Attribution (CC BY) license (<https://creativecommons.org/licenses/by/4.0/>).

1. Introduction

Femtosecond fiber lasers, with their ultra-high peak power density, extremely short pulse duration, broad spectrum, excellent environmental stability [1], etc., play an important role in fields such as communication [2], military [3], and medical treatment [4], etc. As a typical nonlinear dissipative system, erbium-doped femtosecond fiber lasers have also become an ideal platform for exploring soliton dynamics [5], facilitating the observation of a wide range of soliton phenomena. Fibers typically have a limited mode field area. When the peak power reaches a certain threshold, due to the soliton area theory and the quantization effect of pulse energy [6], laser pulses undergo soliton break-up and interact to form higher-order solitons. Among these, bound-state solitons represent a distinct manifestation of higher-order solitons, comprising soliton bundles formed by two or more sub-pulses that are coupled through nonlinear interactions. These sub-pulses exhibit mutual attraction when they deviate significantly from their equilibrium distance, and conversely, they repel each other when they come closer [7]. The temporal spacing between adjacent sub-pulses plays a pivotal role in the formation of bound-state solitons [8]. This parameter allows for the classification of bound states into two categories: loosely bound [9] and tightly

bound states [10]. Loosely bound states refer to configurations where the spacing between adjacent solitons exceeds several pulse widths. Additionally, it has been found that the soliton pairs can also act as a unit to form other bound states of solitons, such as the $(2 + 2)$, $(2 + 1)$, and $(2 + 2 + 2)$ configurations [11]. Currently, bound states have been utilized to improve low-order harmonics and for the generation of higher-order optical harmonics in the design of photonic devices. By applying bound states, light-matter interactions hold the potential for designing solid-state attosecond spectroscopy and ultraviolet source technologies. Furthermore, through bound states, quantum confinement effects are being explored to leverage optical properties for applications in quantum information processing, particularly in the design of qubits and nonlinear quantum computations [12].

Despite the considerable attention and extensive studies on bound-state solitons, their regulation remains challenging in conventional optical media, primarily due to the limited availability of tunable system parameters [13]. To address this, researchers have explored various approaches to control the dynamics of bound-state solitons. For example, Nguyen et al. employed periodic phase modulation to generate phase chirp of the generated lightwaves in the ring laser. Their work revealed that the chirped phase state not only facilitates the formation of multi-soliton-bound states but also enhances their stability [14]. Qin et al. utilized the Rydberg-EIT system to generate nonlocal Kerr nonlinear effects, successful generation, and manipulation of high-dimensional weak-light soliton molecules [13]. While various approaches have been explored for the formation and control of intracavity bound solitons, the use of SAs with exceptional properties offers a more convenient method for achieving bound-state soliton regulation [15]. For example, Liu et al. utilized a carbon nanotube-based SA in a fiber laser and achieved dual-soliton states with discrete equilibrium distances by employing narrowband filtering through a fiber Bragg grating [16]. Similarly, Wang et al. implemented VSe_2/GO SA in a fiber laser and successfully generated soliton molecules by modulating the polarization controller and pump power [17]. Nonetheless, studies focusing on soliton control through SAs and pump power remain limited.

In recent years, chromium disulfide (Cr_2S_3), as a member of transition metal chalcogenides, has garnered significant attention due to its exceptional nonlinear optical properties [18]. At the same time, the application of Cr_2S_3 in the field of lasers has also been demonstrated, showing outstanding performance [19,20]. Its nonlinear photoresponses exhibit minimal dependence on film thickness variations [21] and hold great potential for the design of advanced optoelectronic devices, such as saturable absorbers [20]. Compared to other two-dimensional materials, such as black phosphorus, Cr_2S_3 offers excellent optical stability in ambient environments [22]. We compare three key characteristics of typical two-dimensional materials' SAs: bandgap, responsivity, and the pulse width of mode-locked lasers based on these SAs, as shown in Figure 1. In this figure, the parameters of the three characteristics are normalized, and an axial coordinate system is established. The relative magnitude of each parameter is represented by the length of the corresponding sector component. In terms of responsivity, materials with higher response rates demonstrate the potential to achieve mode-locking under weaker optical signals. Cr_2S_3 demonstrates a response rate of $3 \text{ A} \cdot \text{W}^{-1}$ under ambient conditions at a central wavelength of 1550 nm [22], second only to carbon nanotubes, which have a response rate of $7.2 \text{ A} \cdot \text{W}^{-1}$ [23], and significantly outperform other commonly used materials such as Graphene, SnS_2 , and Bi_2Te_3 , etc. The bandgap of a material significantly influences the wavelength and range of mode-locked solitons. Cr_2S_3 , with a direct bandgap of approximately 0.15 eV [22], fills the gap between the near-zero bandgap of single-walled carbon nanotubes and the relatively large bandgaps of transition metal dichalcogenides [24]. This property endows Cr_2S_3 with exceptional and highly efficient saturable absorption capabilities in the $1.5 \mu\text{m}$ (0.83 eV)

wavelength region, supporting ultrashort femtosecond pulse durations [20]. In terms of soliton mode-locking pulse width, Yang et al. successfully fabricated a Cr_2S_3 -based SA in 2022 and observed traditional soliton mode-locking as well as triple-pulse bound soliton operation in an erbium-doped fiber laser. The pulse width and time-bandwidth product (TBP) were measured to be 4.60 ps and 2.36, respectively, due to the presence of a large frequency chirp in the mode-locked soliton [20]. In 2024, Qiao et al. investigated Cr_2S_3 -based Q-switched and mode-locked fiber lasers, reporting a mode-locked pulse with a duration of 10.2 ns [19]. A comparison of the mode-locked pulse widths of several saturable absorbers reveals that the Cr_2S_3 SA in this study generates a mode-locking pulse width of 329 fs, which is significantly shorter than that of most other saturable absorbers, reflecting the superior performance of this SA. These findings underscore the exceptional potential of Cr_2S_3 in generating femtosecond lasers and regulating soliton-bound states. However, there is limited research on this saturable absorber in passive mode-locked fiber lasers. It is highly significant to deeply explore the formation and evolution of mode-locked solitons and bound solitons in femtosecond fiber lasers based on Cr_2S_3 SA through numerical simulations.

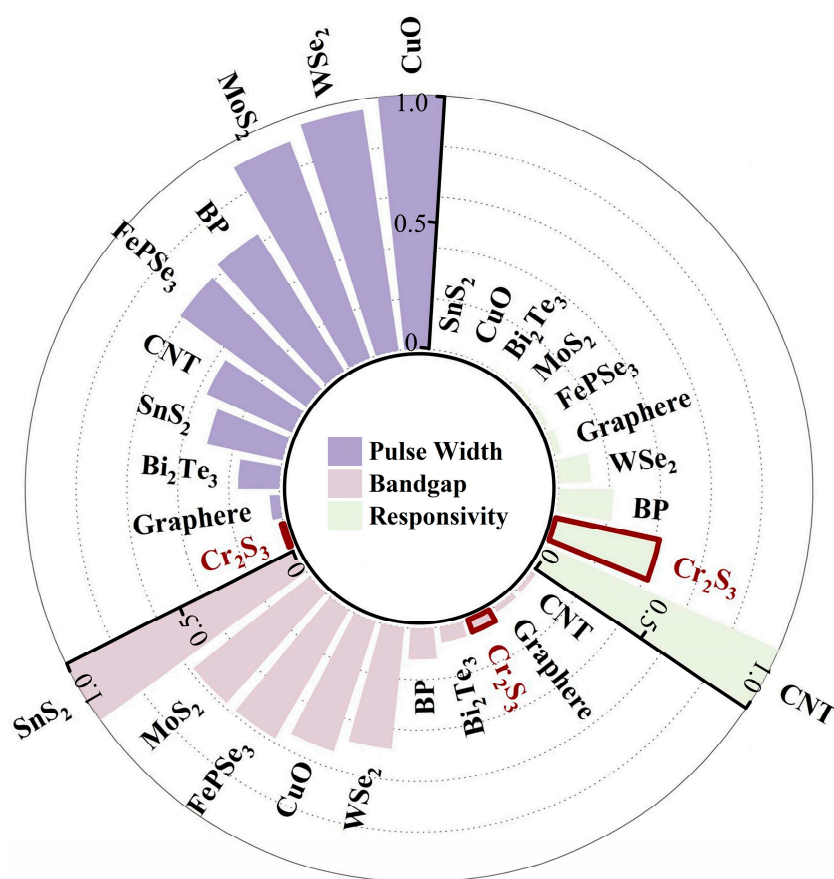


Figure 1. Comparison of commonly used saturable absorbers in terms of bandgap energy (pink), responsivity (green), and mode-locked pulse width (purple). All parameters are normalized for clarity. Data for bandgap energy and responsivity are referenced from [23,25–33], while mode-locked pulse widths are compiled from [34–42]. The three characteristics of the materials in this study are labeled in the figure.

In this work, a physical model for ultrafast soliton evolution based on Cr_2S_3 SA was established. By designing and optimizing the cavity structure, femtosecond-level mode-locked pulses were theoretically achieved, and a wealth of bound soliton phenomena was observed. Based solely on the exceptional characteristics of the SA and the adjustment of

the intracavity gain, mode-locked solitons with a pulse width of 329 fs were achieved in the simulation, with the corresponding TBP of 0.332. Using the designed cavity structure, multi-bound soliton evolution was realized by controlling the small-signal gain coefficient proportional to the pump power, leading to the formation of double-bound solitons and unique (2 + 1) triple-bound solitons. Numerical simulations reveal the evolution process of bound solitons, systematically simulating and analyzing the transitional evolution between different soliton states, thereby theoretically validating the feasibility of this regulation method.

2. Numerical Model of Erbium-Doped Fiber Laser Based on Cr₂S₃-SA

To simulate the soliton evolution within a fiber laser, the numerical cavity model is established based on the modified nonlinear Schrödinger equation:

$$\frac{\partial A}{\partial z} + \frac{i}{2}(\beta_2 + igT_2^2)\frac{\partial^2 A}{\partial T^2} = \frac{1}{2}(g - \alpha)A + i\gamma|A|^2A \quad (1)$$

In this equation, A is the electric envelope of the pulse, β_2 represents the second-order dispersion parameter of the fiber, α corresponds to the attenuation coefficient, and γ is the nonlinear coefficient. The pulse propagation in the cavity is solved using the split-step Fourier method [43]. Under the action of the intracavity gain and the saturable absorption effect caused by the nonlinear device, the dominant pulse, that is, the soliton, gradually forms. The parameter T_2 , associated with the gain bandwidth (Ω_g) of the gain fiber, is defined as follows:

$$T_2 = 1/\Omega_g \quad (2)$$

Considering the gain spectrum range of erbium-doped fiber (EDF), Ω_g is set to 40 nm [44]. The nonlinear coefficient γ is defined as follows:

$$\gamma = \omega_0 n_2 / (cA_{\text{eff}}) \quad (3)$$

where ω_0 is the central frequency, n_2 is the nonlinear refractive index, c is the speed of light, and A_{eff} is the effective mode area. The saturated gain coefficient of the active fiber, g is calculated [45] as follows:

$$g = \frac{g_0}{1 + \frac{E_0}{E_{\text{sg}}}} \quad (4)$$

Here, E_0 is intracavity pulse energy, E_{sg} corresponds to the gain saturation energy, with a model value of 1.4 nJ, and g_0 represents the small-signal gain coefficient determined by the pump power, expressed as follows:

$$g_0 = P_p A = P_p \frac{\Gamma_s \sigma_s \Gamma_p \sigma_p}{A_{\text{eff}} h v_p} \quad (5)$$

In this expression, Γ_s and Γ_p are the overlap factors for the signal and pump light, respectively, σ_s and σ_p denote the cross-sections at the transition frequencies of the signal and pump light, P_p is the pump power, h is Planck's constant, and v_p is the pump frequency. Consequently, the small-signal gain coefficient is directly proportional to the P_p . E_0 is computed as follows:

$$E_0 = \int |A|^2 dT \quad (6)$$

As an essential component in mode-locked femtosecond fiber lasers, the SA exhibits a decreasing absorption coefficient as the light intensity increases. The transmission rate t_1 of the SA to the light field is modeled by the following fitted equation [46]:

$$t_1 = 1 - \frac{\Delta T}{1 + \left(\frac{E_0}{E_s}\right)} - \alpha_{ns} \quad (7)$$

In the equation, ΔT is the modulation depth of the SA, E_s is the saturation intensity of the SA, and α_{ns} denotes the nonsaturable loss. To make the Cr_2S_3 SA used in the model more realistic, the modulation depth, nonsaturable loss, and saturation intensity in the model are set based on the data measured in [20], which are 6.36%, 34.99%, and 10.24 MW/cm^2 , respectively.

At the initial stage of mode-locked fiber laser operation, the intracavity optical signal is relatively weak and dominated by high-frequency noise, containing multiple frequency components. Thus, in the simulation, the initial pulse is modeled as a Gaussian pulse with random noise. Since achieving mode-locking requires synchronization of a single transverse mode and multiple longitudinal modes within the cavity, the amplitudes and phases of the longitudinal modes are initially random. Consequently, this leads to a relatively oscillating and chaotic state within the cavity. Based on this analysis, a Gaussian pulse with random noise is employed as the initial signal input for cavity simulations. As light circulates within the cavity, the stronger light can be amplified by the SA, and the weaker light is absorbed by the SA. Eventually, the interplay of dispersion, self-phase modulation (SPM), and gain and loss mechanisms drive the fiber laser to evolve from an initial unstable Gaussian noise pulse into a stable mode-locked pulse.

The initial Gaussian pulse with random noise can be expressed as follows:

$$A(t) = \sqrt{P_0} \left[NLrand(1, M) + e^{-\frac{1}{2}(1+iC_0)(t/T_0)^2} \right] \quad (8)$$

where P_0 is the peak power, NL is the noise level, M is the number of data points, T_0 is the pulsewidth, and C_0 is the chirp of the initial Gaussian pulse. The initial value of those parameters is shown in Table 1, including the time-domain window T_{\max} , the central wavelength λ_0 , and the pulse full-width of half maximum (T_{FWHM}).

Table 1. Initial pulse parameters.

Parameter	Value
λ_0/nm	1550
T_{\max}/ps	60
M	2^{10}
NL	0–1
$T_{\text{FWHM}}/\text{ps}$	10
C_0	0

The central wavelength is selected as 1550 nm due to the higher gain coefficient and broader gain bandwidth of erbium-doped fibers at this wavelength, which enables efficient amplification of optical signals. These characteristics promote the generation and stable propagation of mode-locked solitons and bound-state solitons. Additionally, the 1550 nm wavelength lies within the low-loss window of fibers, rendering it particularly advantageous for optical communication systems [47]. The relationship between T_{FWHM} and T_0 is expressed as follows:

$$T_0 = \frac{T_{\text{FWHM}}}{2\sqrt{\ln(2)}} \quad (9)$$

The parameter NL can be adjusted between 0 and 1 without impacting the simulation results [48]. Additionally, the T_{FWHM} of the initial noise is set to 10 ps because the initial noise only plays a role in the early stage, while the characteristics of the final stable mode-locked pulse are determined by the interplay of gain, loss, SPM, and dispersion during cavity evolution. As such, variations in the T_{FWHM} within a reasonable range do not affect the simulation outcomes. Moreover, 10 ps serves as a threshold between wide-pulse and narrow-pulse evolution, enabling the evaluation of the model's tendency to transition toward narrow pulses or experience pulse break-up under varying conditions, thus facilitating the analysis of the nonlinear optical system's stability [49].

To evaluate the accuracy of the proposed model, a corresponding simulation framework is constructed based on the experimental setup, fiber parameters, and central wavelength reported by Yang et al. [20]. A comparison between the experimental and simulated results was performed. As shown in Figure 2a,b, the mode-locked soliton observed in the experiment exhibited a pulse width of 4.60 ps and a spectral bandwidth of approximately 4 nm, yielding a TBP of 2.36. The simulated results under the corresponding parameters, presented in Figure 2c,d, reveal mode-locked solitons with a pulse width of 4.61 ps and a spectral bandwidth of 4.04 nm. The comparison in Figure 2 demonstrates excellent agreement between the experimental and simulation results, thereby validating the accuracy of the proposed model. This model can thus serve as a reliable tool for investigating pulse evolution dynamics in fiber lasers.

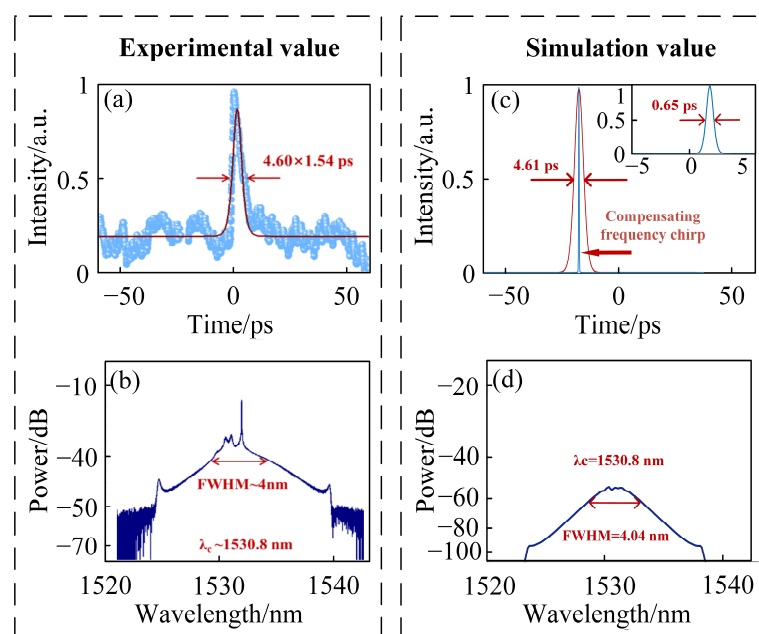


Figure 2. (a) Experimentally obtained mode-locked soliton pulse width and (b) spectral bandwidth [20]; (c) simulated mode-locked soliton pulse width and (d) spectral bandwidth.

In this simulation, the mode-locked pulse exhibits a pulse width of 4.61 ps and a corresponding spectral bandwidth of 4.04 nm, indicating significant frequency chirp accumulation within the pulse. Through calculation, the chirp amount within the pulse is determined to be 7.49 [43]. Furthermore, by compensating for the intra-cavity chirp, the final mode-locked pulse width achieved is 0.65 ps, as illustrated in the inset of Figure 2c. The corresponding TBP is 0.336, which is close to the theoretical transform-limited value.

The introduction of substantial net negative dispersion within the cavity results in a relatively broad mode-locked soliton pulse. Further reduction of the net dispersion in the cavity is advantageous for narrowing the pulse width of mode-locked solitons. Based on this premise, a laser simulation model is designed, as illustrated in Figure 3.

A 0.5 m high-doped polarization-maintaining EDF serves as the gain medium, with a 980 nm laser diode providing the pump source. The pump light is coupled into the laser via a 980/1550 nm wavelength division multiplexer. The cavity is constructed entirely with polarization-maintaining fiber components. After passing through a fiber isolator to ensure unidirectional pulse propagation, the intracavity signal with a central wavelength of 1550 nm is extracted via an 80:20 coupler. Most of the laser is directed through the SA for pulse modulation based on its saturable absorption characteristics, while a small portion is output through the coupler to complete the fiber laser ring cavity.

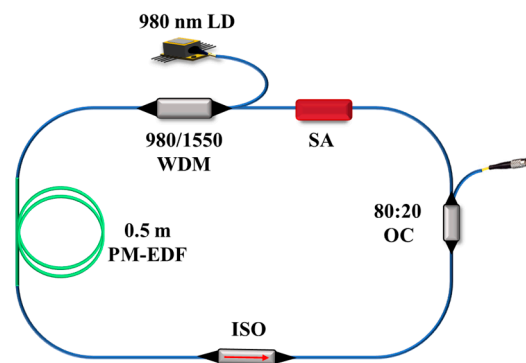


Figure 3. Schematic diagram of the fiber laser model based on Cr₂S₃ SA.

Table 2 summarizes the parameters of the active fiber and passive single-mode fiber (SMF) used in the simulation. The total length of the SMF is set to 2.05 m, achieving a net dispersion of -0.035 ps^2 within the cavity. The entire cavity length is 2.55 m. The pulse repetition frequency in the cavity is determined by the following formula [7]:

$$f = \frac{c}{nL} \quad (10)$$

where n is the refractive index of the fiber, and L denotes the total cavity length, corresponding to a fundamental repetition frequency of 80.5 MHz. Since the pulse width is typically related to the recovery time of the saturable absorber, and the observed soliton pulse width of 4.60 ps is consistent with a fast recovery time [20], we infer that the recovery time of the Cr₂S₃ SA used in our system is also on the ps scale.

Table 2. Fiber parameters.

Fiber Type	$\beta_2/\text{ps}^2/\text{km}$
EDF	23.495
SMF	−22.86

The pulse evolution process in mode-locked fiber lasers is highly dependent on the pump power. In this numerical model, when the pump power-related value g_0 increases, the nonlinear effects within the cavity become prominent. When g_0 reaches the mode-locking threshold, the laser cavity transitions into a stable mode-locked state under the combined influence of dispersion and SPM.

Theoretically, increasing the pump power can generate additional bound states of solitons, attributed to the interplay between the soliton area theorem and pulse energy quantization effects. Soliton break-up only occurs when the pump power reaches a sufficiently high level [50]. The soliton area formula is given by the following [47]:

$$A_0 T_{\text{FWHM}} = \sqrt{\frac{2|D|}{\delta}} \quad (11)$$

In the soliton area equation, A_0 represents the peak amplitude of the pulse, D denotes the net dispersion within the cavity, and δ accounts for the contribution of SPM in the Kerr medium.

Once the optical cavity is established, parameters such as dispersion and nonlinearity in the equation remain constant, resulting in a fixed product of pulse peak amplitude and pulse duration. As is commonly known, increasing the pump power results in a reduction in pulse width. However, constrained by the relaxation time of the Cr_2S_3 SA, the pulse width ceases to decrease further once the limit is reached. At this stage, if g_0 is further increased, the peak amplitude rises. According to the soliton area Formula (11), the peak amplitude cannot increase indefinitely, resulting in soliton break-up. This phenomenon is validated later in the text.

3. Numerical Simulations and Results

3.1. Soliton Mode-Locking

Based on the constructed physical model and the parameters of the Cr_2S_3 SA, an optimized cavity design, as depicted in Figure 3, is developed to maintain a net dispersion of -0.035 ps^2 within the cavity. By controlling the intracavity gain, the rich nonlinear effects are adjusted, thereby revealing the pulse evolution within the cavity. The pulse evolution process in the fiber laser is characterized in terms of roundtrip time and the number of roundtrips.

By incrementally increasing the small-signal gain coefficient in steps of 0.001 to simulate an increase in pump power, a stable mode-locked state is achieved when the small-signal gain coefficient reaches 1.630. The resulting pulse width, as shown in Figure 4a, is determined to be 329 fs via sech-shaped fitting. The corresponding 3 dB spectral bandwidth is measured at 8.12 nm, with Kelly sidebands appearing on both sides of the central wavelength, as illustrated in Figure 4b. These features are characteristic of soliton mode-locking, confirming the generation of the mode-locked pulse within the cavity. The calculated TBP of the mode-locked soliton is 0.332, closely approaching the theoretical transform-limited value, indicating that the soliton exhibited only minimal nonlinear chirp. The real-time evolution of the soliton is depicted in Figure 4c. As seen in the figure, mode-locking commences after approximately 70 cavity roundtrips. However, due to the imbalance between gain and loss within the cavity, the peak power of the mode-locked pulse exhibits oscillations. After 160 roundtrips, the pulse intensity gradually stabilizes and remains constant, reflecting the establishment of a stable mode-locked state.

By further increasing the pump power, the intracavity optical intensity rises, enhancing the nonlinear effects, particularly SPM, which is proportional to the optical intensity. This enhancement of SPM generates additional frequency components, leading to spectral broadening, as illustrated in Figure 5a. As the spectrum broadens, the mode-locked pulse width correspondingly decreases. However, due to the relaxation time limitation of the Cr_2S_3 SA, the pulse width stabilizes at 242 fs when $g_0 = 1.750$. The increased nonlinear effects within the mode-locked soliton result in the TBP deviating progressively from the theoretical transform-limited value. This indicates an increase in the nonlinear chirp of the mode-locked soliton, leading to a gradual destabilization of the soliton. The relationship between the TBP of the soliton and the small-signal gain coefficient g_0 is shown in Figure 5b.

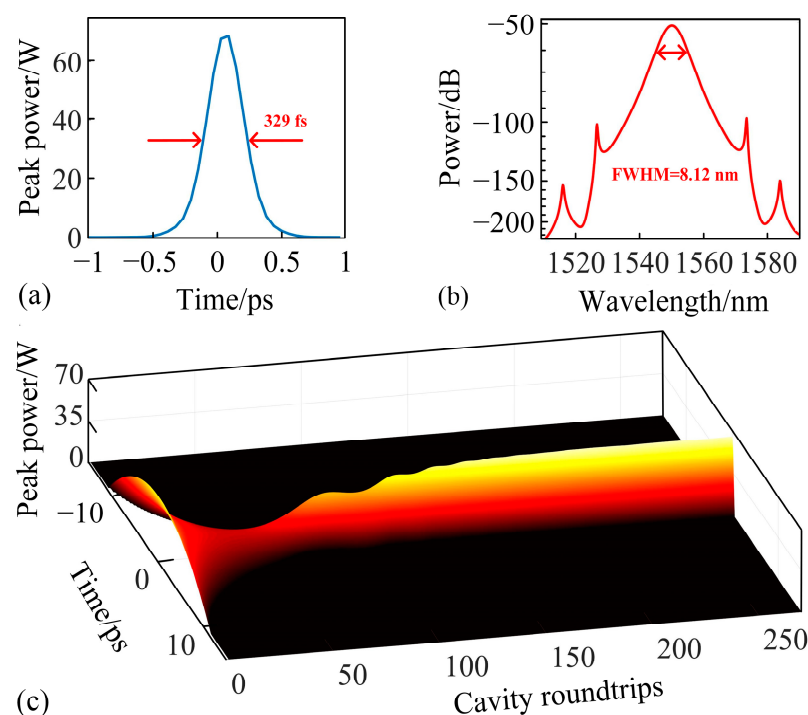


Figure 4. (a) Temporal profile of the mode-locked pulse at $g_0 = 1.630$ after achieving stable mode-locking; (b) corresponding optical spectrum of the mode-locked soliton; (c) real-time evolution of the soliton from initial noise to stable mode-locking state.

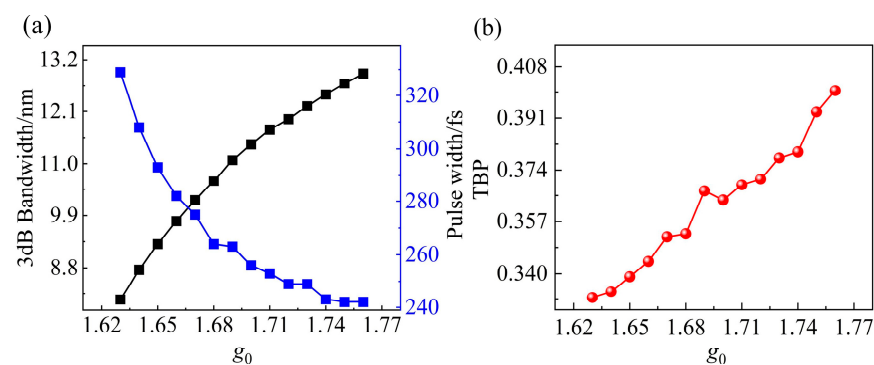


Figure 5. (a) Variation of the 3 dB spectral bandwidth (black) and mode-locked pulse width (blue) as a function of the small-signal gain coefficient g_0 ; (b) evolution of TBP with g_0 . As g_0 increases, the TBP deviates from the transform-limited value, reflecting the impact of gain narrowing on pulse quality.

3.2. Soliton Transition Phase

As the gain coefficient gradually increases, the cumulative intracavity nonlinearity, combined with pulse shaping by the SA and modulation by the soliton area theorem [6], leads to the break-up of a single soliton into multiple solitons. Stronger gain amplifies small signals, such as background noise, into sub-pulses, causing the pulse to split into double solitons or multiple solitons. During propagation within the cavity, the break-up solitons experience attractive and repulsive forces that achieve a state of dynamic equilibrium. In summary, the critical factors for soliton break up into high-order bound solitons include the amplification of small signals, sufficiently strong gain, and the balance of inter-soliton interaction forces. These conditions collectively enable the formation and stabilization of high-order bound solitons within the laser cavity.

During the transition from a single soliton to double solitons, a soliton transition phase is observed, as depicted in Figure 6. This phenomenon has also been reported in previous studies [51]. Figure 6 illustrates the pulse evolution during the transitional

stage under a pump parameter of $g_0 = 1.765$. Initially, the pulse undergoes continuous reshaping while emitting dispersive waves into the background. These dispersive waves can either be amplified or attenuated, depending on the strength of the gain. Once amplified to a sufficiently high level, the pulse experiences break-up, leading to the formation of multiple pulses. After the pulse breaks up, the available gain becomes insufficient to sustain two solitons simultaneously. Under the influence of gain competition [52], the soliton with higher energy secures a greater share of the gain, while the weaker soliton is progressively attenuated and eventually dissipates. As a result, only a single soliton remains. With further cavity roundtrips, the system gradually stabilizes into a steady-state mode-locked operation. In reference [53], the transition from a single pulse to a double pulse phase was achieved under near-zero dispersion conditions, eventually leading to a unique breathing phase. The transition phase in this study ultimately resulted in single soliton mode-locking, which differs from the observations in [53]. This highlights that the transition phases of higher-order solitons vary under different dispersion conditions.

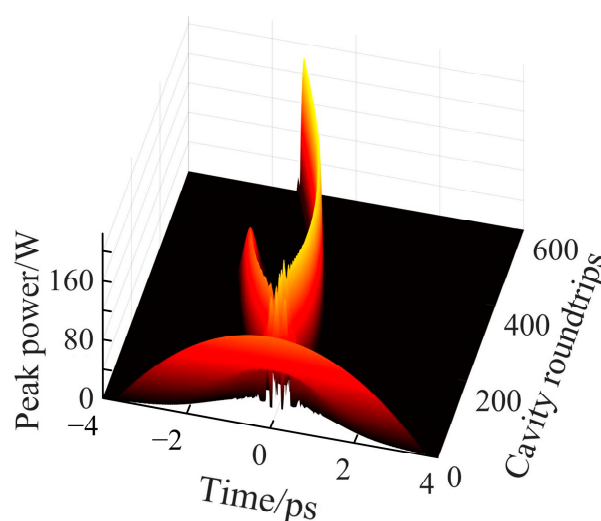


Figure 6. Evolution of the pulse profile during the transition stage at $g_0 = 1.765$. This plot depicts the temporal dynamics of the peak power as a function of cavity roundtrips, highlighting the complex processes of pulse reshaping and stabilization.

3.3. Double-Bound Solitons

As the small-signal gain coefficient g_0 gradually exceeds 1.765, the intracavity gain becomes sufficiently strong to induce soliton to break up into double solitons. However, the spacing between the two solitons remains unstable. This instability arises from an imbalance between the nonlinear and dispersive interaction forces. Additionally, the two solitons perturb each other, resulting in continuous modulation of the oscillation period and variations in their temporal separation.

Figure 7a shows the spectral evolution when $g_0 = 1.770$. Evident interference fringes in the soliton spectrum can be observed, caused by the interference between the two pulses. After 4500 cavity roundtrips, the soliton pair remains unstable. The interference fringes progressively shift toward longer wavelengths, reflecting continuous sliding of the relative phase between the solitons. This persistent instability indicates that the balance between attractive and repulsive forces between the solitons has not yet been achieved, leaving the system in a state of dynamic adjustment. This finding underscores the complex interplay of nonlinear and dispersive effects in governing the evolution of soliton-bound states.

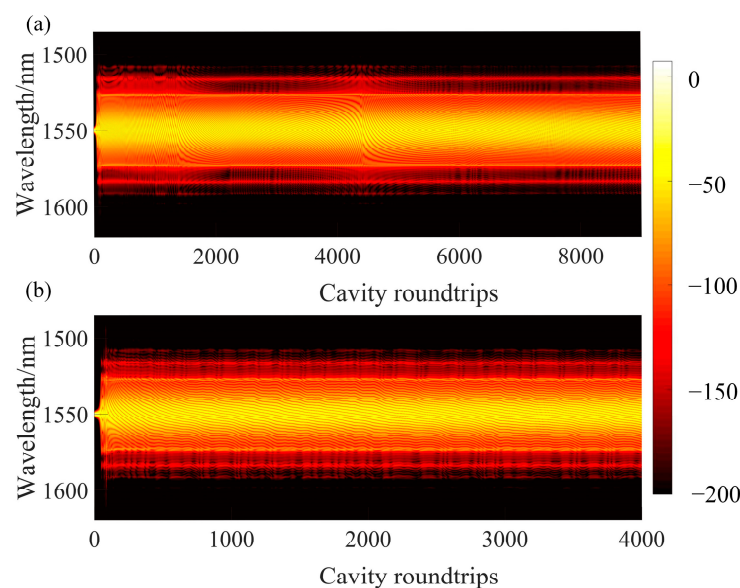


Figure 7. (a) Evolution of the unstable dual-soliton spectrum at $g_0 = 1.770$. The horizontal axis represents the wavelength (nm), and the vertical axis denotes cavity roundtrips. The spectrum evolves within the 1500–1600 nm range over time, exhibiting instability. (b) Evolution of the stable double-bound solitons spectrum at $g_0 = 1.780$. The horizontal axis represents the wavelength (nm), and the vertical axis denotes cavity roundtrips. The spectrum evolves within the 1500–1600 nm range, with the movement of fringe patterns indicating changes in the relative phase, demonstrating the stable characteristics of double-bound solitons.

As the intracavity gain continues to increase, the nonlinear attraction between solitons strengthens, gradually balancing the dispersive repulsion between pulses. When the small-signal gain coefficient $g_0 = 1.780$, the spacing in the soliton pair approaches stability. Due to the effects of dispersion, the spectral evolution, as shown in Figure 7b, exhibits relatively smooth interference fringe variations, reflecting the continuous adjustment of the relative phase between the solitons [54]. After multiple cavity roundtrips, a stable double-bound soliton eventually forms, as illustrated in Figure 8a.

To quantitatively analyze the evolution of soliton spacing during cavity propagation, the separation between the two solitons is measured every 100 cavity roundtrips, and the results are fitted to produce a curve, as shown in Figure 8b. The horizontal axis represents the bound soliton separation, while the vertical axis denotes the number of cavity roundtrips. When the number of cavity roundtrips reaches 4000, the intracavity soliton evolution stabilizes, resulting in the pulse envelopes shown in Figure 9a. The stabilized soliton separation time is approximately 5.17 ps, with each individual soliton having a pulse width of 0.31 ps. Since the soliton separation is approximately 17 times the width of a single soliton, the system achieves a second-order loosely bound soliton state.

As shown in Figure 8b, at 3350 cavity roundtrips, the soliton separation is 5.05 ps, which is relatively small. Under these conditions, the solitons repel each other, leading to an increase in their separation. At 3650 roundtrips, the soliton separation reaches a maximum of 5.40 ps. For this relatively large separation, the solitons attract each other, causing the separation to decrease. By 4000 roundtrips, the pulse spacing stabilizes at 5.17 ps. In all cases, the soliton pair adjusts toward the equilibrium distance, signifying the formation of a stable double-bound soliton state [55]. From the fitted curve, it is evident that once the soliton pair stabilizes, the net negative dispersion within the laser cavity induces periodic interactions between the solitons and the cavity dispersion. These interactions result in periodic perturbations of the solitons, maintaining a dynamic equilibrium in the spacing between the soliton pair. The intracavity pulse evolution is extended to 5000 cavity

roundtrips to analyze the fluctuation range of the separation between loosely bound solitons. As shown in the illustration of Figure 8b, the results indicate that the soliton separation fluctuations remained within a range of ± 0.5 ps. This demonstrates that the system exhibits satisfactory stability. The result in this paper is similar to that reported in reference [56], which demonstrated quasi-periodic pulsating pure-quartic solitons (PQS) molecules. The quasi-periodic pulsation feature of the PQS molecules is characterized by small oscillations of ± 0.4 ps around a distance of approximately 12.5 ps between two pulses. In contrast, the bound soliton pulse spacing in this study is even smaller, leading to stronger interactions.

In the spectral profile shown in Figure 9b, Kelly sidebands are still evident. These sidebands arise when the small-amplitude dispersive waves emitted by the pulse satisfy the phase-matching condition with the cavity's free spectral range. Dispersive waves are generated as the pulse undergoes periodic gain and loss perturbations during cavity circulation, leading to periodic self-reshaping and energy release.

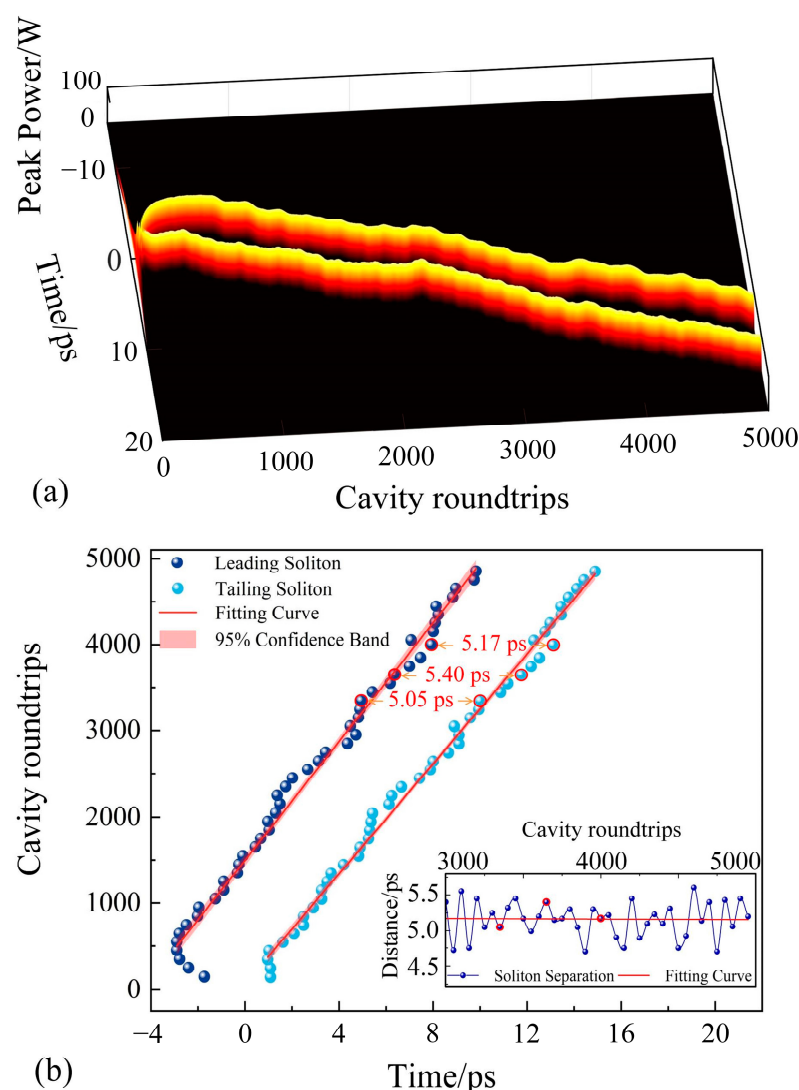


Figure 8. (a) Evolution diagram of double-bound solitons at $g_0 = 1.780$; (b) sampling diagram of the spacing between double-bound solitons corresponding to (a) (fitted curve based on sampled points). The illustration shows the distance between the two pulses within the double-bound solitons. The red circles correspond to the three sampled points in (b).

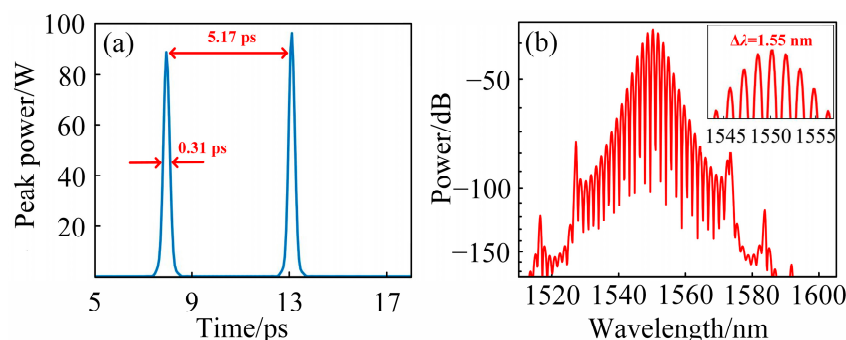


Figure 9. (a) Temporal profile of double-bound solitons after 4000 cavity roundtrips at $g_0 = 1.780$; (b) spectral profile of the double-bound solitons corresponding to (a).

Dispersive waves can mediate periodic interactions between solitons based on their initial pulse separation. While other mechanisms, such as laser gain recovery and acoustic effects, have also been reported to introduce weak soliton interactions within lasers, dispersive-wave-mediated soliton interactions are the most significant [57]. These interactions play a critical role in the formation of loosely bound soliton states in lasers. In simple terms, dispersive waves influence the interactions between solitons, linking their phase and spacing. Compared to scenarios without dispersive waves, solitons can interact over relatively larger distances [54].

From the spectrum in Figure 9b, distinct modulation patterns are evident, and the pulse temporal intervals remain relatively constant. According to Fourier transform theory, the spectral modulation ($\Delta\lambda$) of bound-state mode-locked pulses and the pulse time interval (ΔT) satisfy the following equation [6]:

$$\Delta T = \frac{\lambda_0^2}{c\Delta\lambda} \quad (12)$$

By measuring the spectral modulation period as 1.55 nm, the corresponding pulse interval is calculated to be 5.17 ps using this equation. This result aligns well with the pulse interval measured in the simulation shown in Figure 9a, further confirming that the observed dual pulses correspond to double-bound solitons.

3.4. Triple-Bound Solitons

By gradually increasing the gain coefficient g_0 in steps of 0.001, the nonlinear effects within the cavity further intensify. During this process, the evolution of solitons displays transitional states similar to those observed in the soliton transition phase described in Section 3.2. At $g_0 = 1.930$, the solitons transition from an initial three-pulse configuration to a two-pulse configuration, indicating that $g_0 = 1.930$ serves as the threshold for the generation of three solitons. This observation also demonstrates that the soliton transition process is not limited to the transformation from a single soliton to a two solitons state but may occur at each step of forming higher-order solitons.

As the pump power continues to increase, the spectrum exhibits pronounced double interference fringes at $g_0 = 1.940$, as shown in Figure 10a. With the stabilization of the solitons, a unique triple-bound solitons are observed [11]. Unlike the conventional triple-bound solitons with equal pulse intervals, this configuration features unequal spacing between the solitons, as illustrated in Figure 10b. In this figure, the horizontal axis represents the number of cavity roundtrips, while the vertical axis denotes the temporal intervals between solitons.

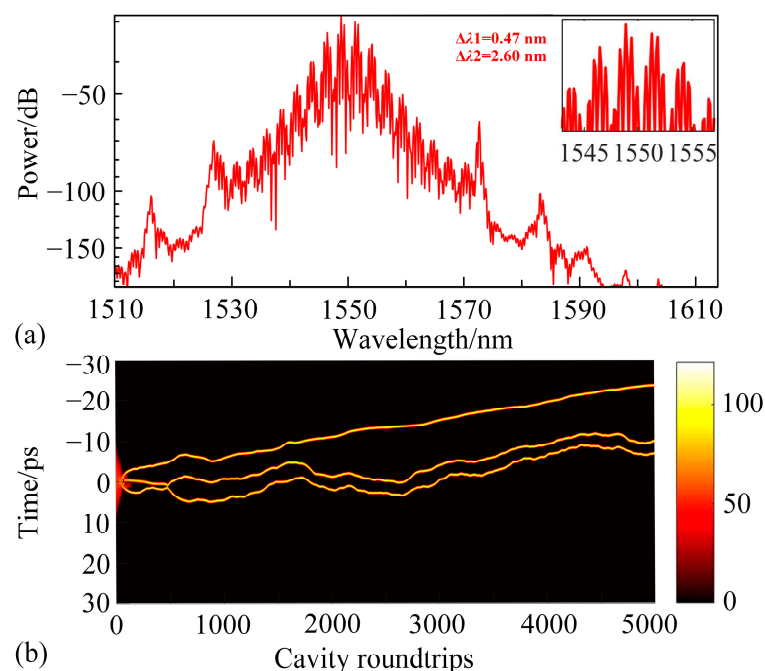


Figure 10. (a) Spectrum of the triple-bound solitons after 5000 cavity roundtrips at $g_0 = 1.940$; (b) Pulse evolution of the triple-bound solitons at $g_0 = 1.940$.

This bound state consists of a soliton pair and a single soliton, with the interval between the soliton pair remaining constant after stabilization. This is due to the strong nonlinear interaction between the closely spaced pulses, which allows the bound soliton pair to stably propagate as a single unit. Considering that dispersive waves induce positional oscillations of individual solitons, this is also the reason for the random fluctuations in the positions of the soliton pair, corresponding to periodic jitter. From the spectral plot of this bound state, it is observed that the spectrum undergoes dual modulation with spectral periods of $\Delta\lambda_1 = 0.47 \text{ nm}$ and $\Delta\lambda_2 = 2.60 \text{ nm}$, respectively. The modulation period $\Delta\lambda_1 = 0.47 \text{ nm}$ varies within each pulse cycle, resulting in changes in the interval between the single soliton and the soliton pair. However, the modulation period $\Delta\lambda_2 = 2.60 \text{ nm}$ remains constant throughout the pulse cycle, leading to the formation of a 2 + 1 type triple-bound solitons.

From the pulse evolution diagram of the bound solitons, it is evident that the distances between the three solitons are unequal. The possible reasons for this can be attributed to two factors. On the one hand, the solitons in the fiber laser undergo periodic amplification, loss, and output, which may result in different interactions between the three solitons. On the other hand, as the solitons propagate in the fiber laser, dispersive waves are generated, and the interaction between the dispersive waves and the solitons also occurs within the laser cavity. However, due to the periodic effects in the fiber laser, the interactions between the solitons and the dispersive waves may differ, leading to unequal spacing between the three coupled solitons along the time axis [58].

Finally, since the output pulse energy increases proportionally with g_0 , the maximum output pulse power is reached when $g_0 = 1.940$. By combining this with the pulse repetition frequency inside the cavity, the intracavity power density is calculated to be slightly lower than the experimental value in reference [20]. Therefore, the phenomenon observed in this study is not affected by optical damage. Meanwhile, in a polarization-maintaining fiber cavity, the relative angle between the initial polarization state and the fiber's principal axes may still introduce additional degrees of freedom in soliton dynamics through nonlinear birefringence modulation [59]. This study employs an initial Gaussian noise pulse (with its

polarization direction aligned with the slow axis by default) to focus on the dominant roles of gain, dispersion, and nonlinear effects in soliton formation and bound-state evolution.

4. Conclusions

In this work, we establish a physical model for soliton propagation in femtosecond fiber lasers based on Cr₂S₃ SA, further revealing the formation and evolution of mode-locked solitons, soliton transition states, and high-order bound solitons. By optimizing the cavity structure to reduce the net dispersion, the pulse width of the mode-locked soliton is reduced to 329 fs, with a corresponding TBP of 0.332. Through the gradual increase of the small-signal gain coefficient g_0 , which corresponds to the pump power, the transition from mode-locked solitons to high-order solitons is initially observed. Subsequently, stable double-bound solitons are achieved, with the soliton pair maintaining a dynamic equilibrium with a spacing of approximately 5.17 ps. Finally, a (2 + 1) type triple-bound soliton is realized, consisting of a single soliton and a soliton pair, where the spacing between the soliton pair remains unchanged. As the small-signal gain coefficient is further increased, more soliton splitting is due to the peak power effect [60]. These results demonstrate that Cr₂S₃ SA possesses excellent nonlinear properties and holds significant potential as a saturable absorber in ultrafast fiber lasers. This study contributes to the further investigation of the multifunctional characteristics of bound states, offering insights into their interaction mechanisms as well as the design of multifunctional fiber lasers and potential applications in optical information storage and high-capacity optical communication.

Author Contributions: Conceptualization, D.L.; methodology, D.L. and Y.W.; software, R.Z. and Y.W.; validation and formal analysis, D.L., R.Z., M.L., K.Z., Q.Y. and Y.W.; investigation, D.L., X.W., X.L. and Y.D.; resources, R.Z. and Y.W.; data curation, D.L. and Y.W.; writing—original draft preparation, D.L.; writing—review and editing, M.L., Y.W., K.Z. and R.Z.; visualization, D.L., Y.W., X.W., X.L. and Y.D.; supervision, R.Z. and Z.J.; project administration, R.Z. and Z.J.; funding acquisition, R.Z., M.L., K.Z. and Y.W. All authors have read and agreed to the published version of the manuscript.

Funding: This research was funded by the National Natural Science Foundation of China (grant number 12404485); the Key R&D Program of Shandong Province (grant number 2021CXGC010202); International Cooperation Project of Shandong Province's Key R&D Program (grant number 2024KJHZ025); the General program of the Natural Science Foundation of Shandong Province (grant numbers ZR2022MA046 and ZR2021MF112); and pilot projects for integrating science, education and industry of Qilu University of Technology (Shandong Academy of Sciences) (grant number 2024GH11 and 2024GH13).

Institutional Review Board Statement: Not applicable.

Informed Consent Statement: Not applicable.

Data Availability Statement: The original contributions presented in the study are included in the article, further inquiries can be directed to the corresponding authors.

Conflicts of Interest: The authors declare no conflicts of interest.

References

1. Wang, X.Z.; Wang, Z.H.; Wang, Y.Y.; Zhang, X.; Song, J.J.; Wei, Z.-Y. A Self-Diffraction Temporal Filter for Contrast Enhancement in Femtosecond Ultra-High Intensity Laser. *Chin. Phys. Lett.* **2021**, *38*, 074202. [[CrossRef](#)]
2. Xu, Y.; Xie, H.; Jiang, G.; Miao, L.; Wang, K.; Tang, S.; Yu, X.; Zhang, H.; Bao, Q. Bilayer Bismuth Selenide Nanoplatelets Based Saturable Absorber for Ultra-short Pulse Generation (Invited). *Opt. Commun.* **2017**, *395*, 55–60. [[CrossRef](#)]
3. Yang, L.-M.; Wan, P.; Protopopov, V.; Liu, J. 2 μ m Femtosecond Fiber Laser at Low Repetition Rate and High Pulse Energy. *Opt. Express* **2012**, *20*, 5683. [[CrossRef](#)] [[PubMed](#)]
4. Yanik, M.F.; Cinar, H.; Cinar, H.N.; Chisholm, A.D.; Jin, Y.; Ben-Yakar, A. Functional Regeneration after Laser Axotomy. *Nature* **2004**, *432*, 822. [[CrossRef](#)] [[PubMed](#)]

5. Liu, X.M.; Popa, D.; Akhmediev, N. Revealing the Transition Dynamics from Q Switching to Mode Locking in a Soliton Laser. *Phys. Rev. Lett.* **2019**, *123*, 093901. [\[CrossRef\]](#) [\[PubMed\]](#)
6. Guo, B.; Guo, X.; Zhou, R.; Ren, Z.; Chen, Q.; Xu, R.; Luo, W. Multi-Pulse Bound Soliton Fiber Laser Based on MoTe₂ Saturable Absorber. *Nanomaterials* **2022**, *13*, 177. [\[CrossRef\]](#)
7. Sun, D.; Zhao, Q.; Chu, S.; Cao, C.; Pei, J.; Xu, X.; Ruan, S. Multiple Bound State Soliton Pulses in the All Polarization Maintaining Fiber Laser. *Micromachines* **2023**, *14*, 1528. [\[CrossRef\]](#) [\[PubMed\]](#)
8. Wu, C.H.; Yao, Y.; Yang, Y.; Xu, X.C.; Tian, J.J.; Xu, K. Wavelength-Switchable and Multi-Pulse Bound State Based on a Hybrid Mode-Locked Mechanism. *Opt. Express* **2022**, *30*, 10732. [\[CrossRef\]](#)
9. Li, X.; Xia, K.; Wu, D.; Nie, Q.; Dai, S. Bound states of solitons in a fiber laser with a microfiber-based WS₂ saturable absorber. *IEEE Photonics Technol. Lett.* **2017**, *29*, 2071–2074. [\[CrossRef\]](#)
10. Herink, G.; Kurtz, F.; Jalali, B.; Solli, D.R.; Ropers, C. Real-Time Spectral Interferometry Probes the Internal Dynamics of Femtosecond Soliton Molecules. *Science* **2017**, *356*, 50–54. [\[CrossRef\]](#) [\[PubMed\]](#)
11. Wang, X.; Sun, M.; Liang, Q.; Yang, S.; Li, S.; Ning, Q. Observation of Diverse Structural Bound-State Patterns in a Passively Mode-Locked Fiber Laser. *Appl. Phys. Express* **2020**, *13*, 022009. [\[CrossRef\]](#)
12. Torres-Torres, C.; García-Beltrán, G. Theoretical Models for Describing an Enhancement in Nanoscale Optical Nonlinearities for Applications Design. In *Optical Nonlinearities in Nanostructured Systems*; Springer Tracts in Modern Physics; Springer International Publishing: Cham, Switzerland, 2022; Volume 287, pp. 33–58, ISBN 978-3-031-10823-5.
13. Qin, L.; Hang, C.; Malomed, B.A.; Huang, G. Stable High-Dimensional Weak-Light Soliton Molecules and Their Active Control. *Laser Photonics Rev.* **2022**, *16*, 2100297. [\[CrossRef\]](#)
14. Nguyen, N.D. Generation of High-order Multi-bound Solitons and Propagation in Optical Fibers. *Opt. Commun.* **2009**, *282*, 2394–2406. [\[CrossRef\]](#)
15. Du, Y.; Gao, Q.; He, Z.; Li, J.; Zeng, C.; Mao, D.; Zhao, J. Stable Loosely Bounded Asymmetric Soliton Molecules in Fiber Lasers. *Phys. Rev. A* **2021**, *104*, 043508. [\[CrossRef\]](#)
16. Liu, X.M.; Han, X.X.; Yao, X.K. Discrete Bisoliton Fiber Laser. *Sci. Rep.* **2016**, *6*, 34414. [\[CrossRef\]](#) [\[PubMed\]](#)
17. Wang, B.; Han, H.; Yu, L.; Wang, Y.; Dai, C. Generation and Dynamics of Soliton and Soliton Molecules from a VSe₂/GO-Based Fiber Laser. *Nanophotonics* **2021**, *11*, 129–137. [\[CrossRef\]](#) [\[PubMed\]](#)
18. Hu, J.; Yang, L.; Chen, L.; Huang, J.; Zhu, H.; Miao, L.; Zhao, C. Nanosecond mid-infrared pulse generation modulated by platinum ditelluride nanosheets. *Laser Phys. Lett.* **2022**, *19*, 075107. [\[CrossRef\]](#)
19. Qiao, J.; Zhu, R.; Ahmed, S.; Fan, R.; Ivan, M.N.A.S.; Liu, G.; Tsang, Y.H.; Feng, S. Passive Mode-Locking and Q-Switching of Ytterbium-Doped Fiber Lasers Using Cr₂S₃ Saturable Absorbers. *Opt. Quantum Electron.* **2024**, *56*, 1146. [\[CrossRef\]](#)
20. Yang, F.; Sui, Z.; Sun, S.; Chen, S.; Wang, Y.; Fan, W.; Li, S.; Wang, G.; Zhang, W.; Lu, C.; et al. Demonstration of Conventional Soliton, Bound-State Soliton, and Noise-Like Pulse Based on Chromium Sulfide as Saturable Absorber. *Nanophotonics* **2022**, *11*, 4937–4945. [\[CrossRef\]](#)
21. Fan, X.; Chen, Z.; Xu, D.; Zou, L.; Ouyang, F.; Deng, S.; Wang, X.; Zhao, J.; Zhou, Y. Phase-Controlled Synthesis of Large-Area Trigonal 2D Cr₂S₃ Thin Films via Ultralow Gas-Flow Governed Dynamic Transport. *Adv. Funct. Mater.* **2024**, *34*, 2404750. [\[CrossRef\]](#)
22. Xie, L.; Wang, J.; Li, J.; Li, C.; Zhang, Y.; Zhu, B.; Guo, Y.; Wang, Z.; Zhang, K. An Atomically Thin Air-Stable Narrow-Gap Semiconductor Cr₂S₃ for Broadband Photodetection with High Responsivity. *Adv. Electron. Mater.* **2021**, *7*, 2000962. [\[CrossRef\]](#)
23. Tang, Y.; Fang, H.; Long, M.; Chen, G.; Zheng, Z.; Zhang, J.; Zhou, W.; Ning, Z.; Zhu, Z.; Feng, Y.; et al. Significant Enhancement of Single-Walled Carbon Nanotube Based Infrared Photodetector Using PbS Quantum Dots. *IEEE J. Select. Topics Quantum Electron.* **2018**, *24*, 3801608. [\[CrossRef\]](#)
24. Huang, Z.; Han, W.; Tang, H.; Ren, L.; Chander, D.S.; Qi, X.; Zhang, H. Photoelectrochemical-Type Sunlight Photodetector Based on MoS₂ /Graphene Heterostructure. *2D Mater.* **2015**, *2*, 035011. [\[CrossRef\]](#)
25. Zhang, B.Y.; Liu, T.; Meng, B.; Li, X.; Liang, G.; Hu, X.; Wang, Q.J. Broadband High Photoresponse from Pure Monolayer Graphene Photodetector. *Nat. Commun.* **2013**, *4*, 1811. [\[CrossRef\]](#) [\[PubMed\]](#)
26. Choi, W.; Cho, M.Y.; Konar, A.; Lee, J.H.; Cha, G.; Hong, S.C.; Kim, S.; Kim, J.; Jena, D.; Joo, J.; et al. High-Detectivity Multilayer MoS₂ Phototransistors with Spectral Response from Ultraviolet to Infrared. *Adv. Mater.* **2012**, *24*, 5832–5836. [\[CrossRef\]](#) [\[PubMed\]](#)
27. Xu, Y.; Liu, C.; Guo, C.; Yu, Q.; Guo, W.; Lu, W.; Chen, X.; Wang, L.; Zhang, K. High Performance near Infrared Photodetector Based on In-Plane Black Phosphorus p-n Homojunction. *Nano Energy* **2020**, *70*, 104518. [\[CrossRef\]](#)
28. Liu, J.; Li, Y.; Song, Y.; Ma, Y.; Chen, Q.; Zhu, Z.; Lu, P.; Wang, S. Bi₂Te₃ Photoconductive Detectors on Si. *Appl. Phys. Lett.* **2017**, *110*, 141109. [\[CrossRef\]](#)
29. Tao, Y.; Wu, X.; Wang, W.; Wang, J. Flexible Photodetector from Ultraviolet to Near Infrared Based on a SnS₂ Nanosheet MicroSphere Film. *J. Mater. Chem. C* **2015**, *3*, 1347–1353. [\[CrossRef\]](#)
30. Zheng, Z.; Zhang, T.; Yao, J.; Zhang, Y.; Xu, J.; Yang, G. Flexible, Transparent and Ultra-Broadband Photodetector Based on Large-area WSe₂ Film for Wearable Devices. *Nanotechnology* **2016**, *27*, 225501. [\[CrossRef\]](#) [\[PubMed\]](#)

31. Gao, Q.; Jin, Z.; Qu, L.; Shao, Z.; Liu, X.; Zhang, Y.; Fu, Z.; Huang, Y.; Wang, L.; Feng, W. CuO Nanosheets for Use in Photoelectrochemical Photodetectors. *ACS Appl. Nano Mater.* **2023**, *6*, 784–791. [\[CrossRef\]](#)
32. Han, X.; Xu, G.; Xing, J.; Song, Y.; Sun, Z.; Rong, D.; Ma, F.; Guo, Z.; Feng, B.; Guo, J.; et al. Response Speed-Tunable Photodetectors Based on Hybrid Ternary FePSe₃ Nanoflakes. *Adv. Opt. Mater.* **2023**, *11*, 2300317. [\[CrossRef\]](#)
33. D'yachkov, P.N. Optical Band Gap Energies in Quasi-Metal Carbon Nanotubes. *Russ. J. Inorg. Chem.* **2018**, *63*, 55–60. [\[CrossRef\]](#)
34. Popa, D.; Jiang, Z.; Bonacchini, G.E.; Zhao, Z.; Lombardi, L.; Torrisi, F.; Ott, A.K.; Lidorikis, E.; Ferrari, A.C. A Stable, Power Scaling, Graphene-Mode-Locked All-Fiber Oscillator. *Appl. Phys. Lett.* **2017**, *110*, 243102. [\[CrossRef\]](#)
35. Wang, Y.; Mao, D.; Gan, X.; Han, L.; Ma, C.; Xi, T.; Zhang, Y.; Shang, W.; Hua, S.; Zhao, J. Harmonic Mode Locking of Bound-State Solitons Fiber Laser Based on MoS₂ Saturable Absorber. *Opt. Express* **2015**, *23*, 205. [\[CrossRef\]](#) [\[PubMed\]](#)
36. Chen, Y.; Jiang, G.; Chen, S.; Guo, Z.; Yu, X.; Zhao, C.; Zhang, H.; Bao, Q.; Wen, S.; Tang, D.; et al. Mechanically Exfoliated Black Phosphorus as a New Saturable Absorber for Both Q-switching and Mode-Locking Laser Operation. *Opt. Express* **2015**, *23*, 12823. [\[CrossRef\]](#) [\[PubMed\]](#)
37. Lin, Y.H.; Lin, S.F.; Chi, Y.C.; Wu, C.L.; Cheng, C.H.; Tseng, W.H.; He, J.H.; Wu, C.I.; Lee, C.K.; Lin, G.R. Using N- and P-Type Bi₂Te₃ Topological Insulator Nanoparticles to Enable Controlled Femtosecond Mode-Locking of Fiber Lasers. *ACS Photonics* **2015**, *2*, 481–490. [\[CrossRef\]](#)
38. Niu, K.; Sun, R.; Chen, Q.; Man, B.; Zhang, H. Passively Mode-Locked Er-Doped Fiber Laser Based on SnS₂ Nanosheets as a Saturable Absorber. *Photon. Res.* **2018**, *6*, 72. [\[CrossRef\]](#)
39. Wang, J.; Li, J.; Chen, H.; Zhang, M.; Li, I.L.; Yan, P. Mode-Locked Thulium-Doped Fiber Laser with WSe₂ Based Evanescent Field Interaction. In Proceedings of the 2017 16th International Conference on Optical Communications and Networks (ICOON), Wuzhen, China, 7–10 August 2017; pp. 1–3.
40. Kong, L.; Chu, H.; Li, Z.; Gao, S.; Pan, Z.; Pan, H.; Zhao, S.; Li, D. The Generation of Noise-like Pulses and Various Solitons with CuO Nanorods as a Broadband Saturable Absorber. *J. Alloys Compd.* **2024**, *984*, 173965. [\[CrossRef\]](#)
41. Wang, Y.; Huang, H.; Li, X.; Ma, K.; Zhao, Y.; Chen, Y.; Feng, J.; Liu, J.; Zheng, C. Controllable Soliton Pairs in Few-Layer FePSe₃ Nanosheets-Based Optical-Intensity Modulators. *ACS Appl. Nano Mater.* **2020**, *3*, 7713–7719. [\[CrossRef\]](#)
42. Pawliszewska, M.; Dużyńska, A.; Zdrojek, M.; Sotor, J. Metallic Carbon Nanotube-Based Saturable Absorbers for Holmium-Doped Fiber Lasers. *Opt. Express* **2019**, *27*, 11361. [\[CrossRef\]](#) [\[PubMed\]](#)
43. Agrawal, G.P. *Nonlinear Fiber Optics*; Springer: Berlin/Heidelberg, Germany, 2000; pp. 195–211, ISBN 978-3-540-66918-0.
44. Mears, R.J.; Reekie, L.; Jauncey, I.M.; Payne, D.N. Low-Noise Erbium-Doped Fiber Amplifier Operating at 1.54 μm . *Electron. Lett.* **1987**, *23*, 1026–1028. [\[CrossRef\]](#)
45. Zhang, Z.X.; Luo, M.; Liu, J.H.; Yang, Y.T.; Li, T.J.; Liu, M.; Luo, A.P.; Xu, W.C.; Luo, Z.C. Coherence-Controlled Chaotic Soliton Bunch. *Nat. Commun.* **2024**, *15*, 6148. [\[CrossRef\]](#)
46. Li, W.; Lin, R.; Chen, G.; Geng, G.; Xu, P.; Yang, Y.; Wang, X.; Xu, J. Observation of Three Kinds of Bound Solitons in a Black Phosphorus-Based Erbium Fiber Laser. *Opt. Fiber Technol.* **2024**, *82*, 103617. [\[CrossRef\]](#)
47. Nelson, L.E.; Jones, D.J.; Tamura, K.; Haus, H.A.; Ippen, E.P. Ultrashort-Pulse Fiber Ring Lasers. *Appl. Phys. B* **1997**, *65*, 277–294. [\[CrossRef\]](#)
48. Yang, L.; Yao, C.; Wu, Y.; Wang, X.; Ren, G.; Wang, C.; Li, P. Theoretical Study on Multi-Range Pulsewidth Tuning in a Dissipative Soliton Laser Mode-Locked by a Dirac Semimetal. *AIP Adv.* **2023**, *13*, 045215. [\[CrossRef\]](#)
49. Haus, H.A. Mode-Locking of Lasers. *IEEE J. Sel. Top. Quantum Electron.* **2000**, *6*, 1173–1185. [\[CrossRef\]](#)
50. Tang, D.Y.; Zhao, L.M.; Zhao, B. Multipulse Bound Solitons with Fixed Pulse Separations Formed by Direct Soliton Interaction. *Appl. Phys. B* **2005**, *80*, 239–242. [\[CrossRef\]](#)
51. Zeng, J.; Sander, M.Y. Real-Time Transition Dynamics between Multi-Pulsing States in a Mode-Locked Fiber Laser. *Opt. Lett.* **2020**, *45*, 5. [\[CrossRef\]](#)
52. Tang, D.Y.; Zhao, L.M.; Zhao, B.; Liu, A.Q. Mechanism of Multisoliton Formation and Soliton Energy Quantization in Passively Mode-Locked Fiber Lasers. *Phys. Rev. A* **2005**, *72*, 043816. [\[CrossRef\]](#)
53. Duan, X.; Liu, Y.; Huang, Q.; Gao, Z.; Jin, L. Impact of Small-Signal Gain and Saturation Energy on the Mode-Locking States in an YB-Doped Fiber Laser. In Proceedings of the 2023 Asia Communications and Photonics Conference/2023 International Photonics and Optoelectronics Meetings (ACP/POEM), Wuhan, China, 4–7 November 2023; pp. 1–5.
54. Soto-Crespo, J.M.; Akhmediev, N.; Grelu, P.; Belhache, F. Quantized Separations of Phase-Locked Soliton Pairs in Fiber Lasers. *Opt. Lett.* **2003**, *28*, 1757. [\[CrossRef\]](#) [\[PubMed\]](#)
55. Rohrmann, P.; Hause, A.; Mitschke, F. Two-Soliton and Three-Soliton Molecules in Optical Fibers. *Phys. Rev. A* **2013**, *87*, 043834. [\[CrossRef\]](#)
56. Yang, S.; Zhu, Z.; Qi, Y.; Jin, L.; Li, L.; Lin, X. Internal Motion within Pulsating Pure-Quartic Soliton Molecules in a Fiber Laser. *Chaos Solitons Fractals* **2023**, *172*, 113544. [\[CrossRef\]](#)
57. Zhao, B.; Tang, D.Y.; Shum, P.; Guo, X.; Lu, C.; Tam, H.Y. Bound Twin-Pulse Solitons in a Fiber Ring Laser. *Phys. Rev. E* **2004**, *70*, 067602. [\[CrossRef\]](#) [\[PubMed\]](#)

58. Gan, Y.; Wu, Q.; Yao, Y.; Liu, C.; Fu, Y.; Yang, Y.; Tian, J.; Xu, K. Generation of High-Order Solitons with Order Continuously Adjustable in a Fiber Laser Based on GIMF–SIMF–GIMF Saturable Absorber. *Opt. Commun.* **2021**, *479*, 126441. [[CrossRef](#)]
59. Huang, Q.; Jiang, H.; Jin, L.; Gao, Z.; Hu, G.; Duan, X.; Li, L. The Impact of Saturable Absorber Recovery Time on Hybrid Mode-Locked Fiber Lasers with near Zero Net Dispersion. *Results Opt.* **2023**, *13*, 100551. [[CrossRef](#)]
60. Liang, H.; Wang, Z.; He, R.; Liu, Y.; Li, H.; Ni, L.; Wang, Z. Evolution of Complex Pulse-Bunches in a Bound-State Soliton Fiber Laser. *IEEE Photonics Technol. Lett.* **2018**, *30*, 1475–1478. [[CrossRef](#)]

Disclaimer/Publisher’s Note: The statements, opinions and data contained in all publications are solely those of the individual author(s) and contributor(s) and not of MDPI and/or the editor(s). MDPI and/or the editor(s) disclaim responsibility for any injury to people or property resulting from any ideas, methods, instructions or products referred to in the content.